

On the application of the Fast Multipole Method to Helmholtz-like problems with complex wavenumber

A. Frangi¹ and M. Bonnet²

Abstract: This paper presents an empirical study of the accuracy of multipole expansions of Helmholtz-like kernels with complex wavenumbers of the form $k = (\alpha + i\beta)\vartheta$, with $\alpha = 0, \pm 1$ and $\beta > 0$, which, notwithstanding, arise for a wealth of different physical problems. It is suggested that a simple point-wise error indicator can provide an a-priori indication on the number N of terms to be employed in the Gegenbauer addition formula in order to achieve a prescribed accuracy when integrating single layer potentials over surfaces. For $\beta \geq 1$ it is observed that the value of N is independent of β and of the size of the octree cells employed while, for $\beta < 1$, simple empirical formulas are proposed yielding the required N in terms of β .

Keywords: Fast Multipole Method, Helmholtz problem, complex wavenumber, Gegenbauer addition theorem

1 Introduction

Many problems of physics and engineering can be formulated and numerically solved by means of integral equations. Resorting to fast approaches is then mandatory for the large scale models often required by realistic simulations. Several strategies are available for the fast solution of large-scale boundary element models. Among these, the Fast Multipole Method (FMM) appeared first and is now well-developed.

The FMM is in particular applied to many physical problems governed by equations of Helmholtz type, which arise for e.g. linear acoustics, electromagnetic or elastic waves upon using Fourier transform in time or applying excitations under prescribed-frequency conditions (with the prescribed angular frequency hereafter denoted by ω). All cases involve integral equations whose (scalar or tensorial) kernels are defined, for three-dimensional formulations, in terms of the fundamental

¹ Politecnico di Milano, Milan (Italy), attilio.frangi@polimi.it

² LMS (UMR CNRS 7649), Ecole Polytechnique, Palaiseau (France), bonnet@lms.polytechnique.fr

solution $K(\mathbf{r}) = \exp(ikr)/4\pi r$ and its derivatives. The FMM crucially rests upon expansions of $K(\mathbf{r})$ that allow a separation of variables between the “field” point \mathbf{y} and the “source” point \mathbf{x} (with $\mathbf{r} = \mathbf{y} - \mathbf{x}$), which are available in several forms. These include the multipole expansion, based on the Gegenbauer addition theorem, and the plane-wave expansion of $K(\mathbf{r})$ in diagonal form.

For real values of the wavenumber k , which correspond to wave propagation problems in lossless media, FMMs based on either type of expansion have been extensively studied and implemented. These studies have in particular established that multipole expansions of $K(\mathbf{r})$ are too costly except at low frequencies (because the expansion truncation threshold increases with k , leading to $O(N^2)$ complexity for high frequencies), while plane-wave expansions are well-suited to higher frequencies but break down in the low-wavenumber limit. Both types of formulations are surveyed in e.g. Nishimura (2002) and Gumerov and Duraiswami (2005). It is also known that in the zero-wavenumber (i.e. static) limit an a-priori indication on the number N of multipoles to be employed in truncated expansions in order to obtain a prescribed accuracy in $K(\mathbf{r})$, unaffected by the dimensions of the cells in the octree, is usually available. This nice feature (which ensures a $O(n_{\text{dof}})$ complexity per iteration for multi-level FMMs applied to static problems) is no longer present in frequency-domain formulations (see e.g. Song, Lu and Chew, 1997; Darve, 2000a,b; Chaillat, Bonnet and Semblat, 2008), whose implementation thus becomes substantially complicated by the need to adapt the truncation order to the level of the octree (resulting in a $O(n_{\text{dof}} \log n_{\text{dof}})$ complexity per iteration).

In contrast, only scattered efforts have so far been devoted to FMMs for Helmholtz-type problems involving *complex* wavenumbers k , see e.g. Geng, Sullivan and Carin (2001) for electromagnetic waves in lossy media or Yasuda and Sakuma (2008) for acoustic wave propagation in porous media. Such formulations involve wavenumbers of the form $k = (\alpha + i\beta)\vartheta$ in terms of real constants α, β, ϑ (with $\beta > 0$, $\alpha = 0, \pm 1$, and $\vartheta > 0$) chosen as explained in the ensuing discussion). The paucity of available studies notwithstanding, complex-wavenumber FMMs arise for a number of different physical problems.

First, such equations and kernels arise naturally upon considering wave propagation in lossy media (e.g. soils) in which mechanical or electromagnetic waves are damped. Such (e.g. viscoelastic) materials may be described, within frequency-domain approaches, in terms of linear constitutive relations involving complex moduli. This leads to complex-valued wavenumbers wherein $\vartheta = \omega$, $\alpha = \pm 1$ and $0 < \beta < 1$ (often with a small imaginary part, i.e. such that $\beta \ll 1$), and represents the most direct generalization of Helmholtz-type equations with real wavenumbers. Another class of such problems correspond to parabolic problems involving elliptic partial differential operators in the space variables and first-order time derivatives,

upon using Fourier transform in time or applying excitations at a prescribed frequency. They include heat conduction, transient Stokes flows, and eddy currents, and the associated Green's functions or tensors involve $K(\mathbf{r})$ with $|\alpha| = \beta = 1$ and $\vartheta = \sqrt{\omega}/2$. Transient Stokes flows arise e.g. in connection with the analysis of dissipation in Micro-Systems (see e.g. Frangi, 2005; Frangi, Spinola and Vigna, 2006). Much of the past effort was on improving the efficiency and robustness of quasi-static Stokes-based fast solvers, but now the focus has shifted to addressing more challenging physics. Newer MEMS use higher operating frequencies and finer dimensions, and therefore the effects of unsteady flow and rarefaction can no longer be ignored (see e.g. Ye, Wang, Hemmert, Freeman and White, 2003). Eddy currents arise in many electrical engineering problems and play an important role e.g. in the design of electrical transformers, where one is especially interested in the accurate calculation of losses. This entails solving the Maxwell equations (in eddy-current approximation) in complex, three-dimensional domains with piecewise constant material parameters (i.e. the magnetic permeability, the dielectric permittivity and the conductivity, respectively). For electrical devices operating continuously under alternating current, time-harmonic states are of interest, leading in effect to an elliptic transmission problem for the eddy-current Maxwell equations (see Schmidlin, Fischer, Andjelic and Schwab, 2001 for a \mathbf{H}, ϕ formulation).

Also amenable to the general framework of Helmholtz-type equations is the computation of Casimir forces, which are attractive forces arising between uncharged conductive surfaces in vacuum, a remarkable consequence of quantum electrodynamics first realized by Casimir (1948). Casimir forces are caused by the energy fluctuations of the electromagnetic field. This complex physical phenomenon is now acquiring technological importance, as it has a major role in modern micro- and nano-technologies when the separation gaps between parts enter the submicron range. The precise evaluation of the Casimir force between surfaces involves very difficult computations, based on quantum mechanics concepts. The simplest case, considered in Casimir's original paper, is represented by two infinite perfectly conductive flat plates with zero thickness, parallel to each other. The computation of Casimir forces for geometries different from flat slabs should be performed by means of suitable numerical tools. A technique based on boundary integral equations, involving kernel $K(\mathbf{r})$ in exponentially-decaying form ($\alpha = 0, \beta = 1$), has recently been proposed in Reid, Rodriguez, White and Johnson (2009).

Finally, one may mention that optical tomography (see e.g. Zacharopoulos, Arridge, Dorn, Kolehmainen and Sikora, 2006) also leads to a Helmholtz equation with complex wavenumber (defined in terms of modulation frequency of light and optical parameters of the medium) with $\alpha = -1, \beta > 1$.

The above-summarized wealth of different applications justifies an investigation of

the Fast Multipole Methods for this class of problems. Currently, little is known about e.g. the appropriate non-dimensional frequency ranges of applicability of either multipole-based or plane wave-based expansions, or the choice of truncation order. In this article, an empirical study of multipole expansions of $K(\mathbf{r})$, of the kind known to be suitable for low real wavenumbers, is conducted for complex wavenumbers of the form $k = (\alpha + i\beta)\vartheta$ with $\alpha = \pm 1, 0$, $\beta > 0$ and $\vartheta > 0$, so as to estimate ranges of applicability in terms of ϑd (d denoting a characteristic cell size) and suitable settings for the truncation order N according to the values of α, β . This article is organised as follows. The multipole expansion of $K(\mathbf{r})$ and its implementation are summarized in Sec. 2. Then, the effect on accuracy of the expansion truncation is studied in Sec. 3 in terms of the usual relative error and a weighted relative error E_M accounting for the exponential decay of $K(\mathbf{r})$ for large $\|\mathbf{r}\|$, for values of α, β which are typical of the main applications of Helmholtz-type equations with complex k . In Sec. 4, the actual truncation error observed on two representative examples of single-layer potentials evaluated over BE meshes featuring up to 20 000 elements is compared to the value of E_M for the same truncation parameter. Practical conclusions regarding truncation rules are finally drawn from the results of these numerical experiments in Sec. 5.

2 Formulation

2.1 Multipole expansion

Let us consider the full-space Green’s function $K(\mathbf{r})$ for the Helmholtz equation:

$$K(\mathbf{r}) = \frac{e^{i(\alpha+i\beta)\vartheta r}}{4\pi r} = \frac{e^{ikr}}{4\pi r}, \quad k = (\alpha + i\beta)\vartheta \tag{1}$$

which solves:

$$\Delta K + k^2 K + \delta(\mathbf{r}) = 0$$

Here $r = \|\mathbf{r}\| = \|\mathbf{y} - \mathbf{x}\|$ denotes the distance between a “source” (collocation) point \mathbf{x} and a “field” point \mathbf{y} ; ϑ is a parameter related to frequency; α, β are real parameters which are application-dependent, as discussed in the Introduction.

For a given pole \mathbf{O} , let $\mathbf{r}_x = \mathbf{x} - \mathbf{O}$, $\mathbf{r}_y = \mathbf{y} - \mathbf{O}$ and $r_x = \|\mathbf{r}_x\|$, $r_y = \|\mathbf{r}_y\|$. The Gegenbauer addition theorem (Abramowitz and Stegun, 1964) states that, for $r_x > r_y$

$$\frac{e^{ikr}}{4\pi r} = \frac{ik}{4\pi} \sum_{n=0}^{\infty} \sum_{m=-n}^n (2n+1)(-1)^m I_n^{-m}(k, \mathbf{r}_y) O_n^m(k, \mathbf{r}_x) \tag{2}$$

where, setting $\hat{\mathbf{r}} = \mathbf{r}/r$,

$$O_n^m(k, \mathbf{r}) = h_n(kr)Y_n^m(\hat{\mathbf{r}}) \tag{3}$$

$$I_n^m(k, \mathbf{r}) = j_n(kr)Y_n^m(\hat{\mathbf{r}}) \tag{4}$$

In eqn. (4) j_n is the spherical Bessel function of the first kind (Abramowitz and Stegun, 1964), h_n is the spherical Hankel function of the first kind:

$$h_n(z) = h_n^{(1)}(z) = j_n(z) + iy_n(z)$$

while the spherical harmonics $Y_n^m(\hat{\mathbf{r}})$ are given in terms of the angular spherical coordinates θ, ϕ of a unit vector $\hat{\mathbf{r}}$ by:

$$Y_n^m(\hat{\mathbf{r}}) = \sqrt{\frac{(n-m)!}{(n+m)!}} P_n^m(\cos \theta) e^{im\phi}$$

where P_n^m are the associated Legendre polynomials. Epton and Dembart (1995), Nishimura, Yoshida and Kobayashi (2001), Yoshida (2001) propose an alternative formulation where solid harmonics R_n^m, S_n^m , defined for a generic point $\mathbf{r} = r\hat{\mathbf{r}}$ by

$$R_n^m(\mathbf{r}) = \frac{1}{(n+m)!} P_n^m(\cos \theta) e^{im\phi} r^n$$

$$S_n^m(\mathbf{r}) = (n-m)! P_n^m(\cos \theta) e^{im\phi} \frac{1}{r^{n+1}},$$

and satisfying

$$R_n^{-m} = (-1)^m \bar{R}_n^m \quad S_n^{-m} = (-1)^m \bar{S}_n^m,$$

are employed instead of spherical harmonics in eqns. (3) and (4), to obtain:

$$O_n^m(k, \mathbf{r}) = h_n(kr) \frac{1}{\sqrt{(n-m)!(n+m)!}} S_n^m(\hat{\mathbf{r}}) \tag{5}$$

$$I_n^m(k, \mathbf{r}) = j_n(kr) \sqrt{(n-m)!(n+m)!} R_n^m(\hat{\mathbf{r}}) \tag{6}$$

The main practical improvement brought by using (5), (6) rather than (3), (4) lies with the fact that $R_n^m(\mathbf{r}), S_n^m(\mathbf{r})$ can be recursively evaluated using the Cartesian coordinates of \mathbf{r} , thus avoiding actual recourse to spherical coordinates.

2.2 Implementation details.

Two major numerical issues require specific attention in the FMM implementation: the evaluation of Bessel function with complex argument and the translation operators.

Evaluation of Bessel functions. Even though this result is not explicitly given for a general complex argument in Abramowitz and Stegun (1964), the spherical Bessel function of third kind $h_n(z)$ can be very efficiently evaluated starting from h_0 and h_1

$$h_0(kr) = \frac{e^{ikr}}{ikr} \quad h_1(kr) = -\frac{e^{ikr}}{(kr)^2}(i + kr)$$

by resorting to the ascending three-term-recurrence-relation (TTRR) which is stable:

$$h_n(z) = \frac{2n - 1}{z} h_{n-1} - h_{n-2}$$

In contrast, j_n cannot be evaluated using the ascending TTRR as it blows up for large n (unless $|z|$ is sufficiently large), while the descending TTRR applied to j_n is stable, as suggested in Abramowitz and Stegun (1964), Section 10.5.

Translation operators. Starting from identities provided in Epton and Dembart (1995) and Yoshida (2001), the following results can be shown to hold for the case at hand. First, the Multipole To Multipole (M2M) translation identity reads:

$$I_n^m(k, \mathbf{O}'\mathbf{y}) = \sum_{n'=0}^{\infty} \sum_{\ell}^{\text{step}=2} \sum_{m'} W_{n,n',\ell}^{m,m'} I_{n'}^{-m'}(k, \mathbf{O}\mathbf{y}) I_{\ell}^{m+m'}(k, \mathbf{O}'\mathbf{O}) \tag{7}$$

where \mathbf{O} and \mathbf{O}' denote the old and new pole, respectively, the lower and upper bounds on ℓ and m' are such that

$$\ell_{\min} = |n - n'|, \quad \ell_{\max} = n + n', \tag{8}$$

$$m'_{\min} = \max(-n', -\ell - m), \quad m'_{\max} = \min(n', \ell - m), \tag{9}$$

and “step = 2” refers to the fact that the sum over ℓ is restricted to even values of $n' + n - \ell$. Moreover, the W symbols in eqn. (7) are given by

$$W_{n,n',\ell}^{m,m'} = (2n' + 1)(2\ell + 1)(-1)^{m+n'+\kappa} \begin{pmatrix} n & n' & \ell \\ 0 & 0 & 0 \end{pmatrix} \begin{pmatrix} n & n' & \ell \\ m & m' & -m - m' \end{pmatrix}, \tag{10}$$

where $\kappa = (n' + n - \ell)/2$ and $\begin{pmatrix} j_1 & j_2 & j_3 \\ k_1 & k_2 & k_3 \end{pmatrix}$ denotes the Wigner-3j symbol (Messiah, 1968), which is non-zero only if:

$$|k_i| \leq j_i \quad \text{and} \quad |j_1 - j_2| \leq j_3 \leq j_1 + j_2$$

Then, the Multipole To Local (M2L) translation identity reads:

$$O_n^m(k, \mathbf{O}'\mathbf{x}) = \sum_{n'=0}^{\infty} \sum_{\ell}^{\text{step}=2} \sum_{m'} W_{n,n',\ell}^{m,m'} I_{n'}^{-m'}(k, \mathbf{O}\mathbf{x}) O_{\ell}^{m+m'}(k, \mathbf{O}'\mathbf{O}) \quad (11)$$

Finally the Local To Local (L2L) translation identity is:

$$O_n^m(k, \mathbf{O}'\mathbf{x}) = \sum_{n'=0}^{\infty} \sum_{\ell}^{\text{step}=2} \sum_{m'} W_{n,n',\ell}^{m,m'} I_{n'}^{-m'}(k, \mathbf{O}'\mathbf{O}) O_{\ell}^{m+m'}(k, \mathbf{O}\mathbf{x}) \quad (12)$$

In eqns. (11) and (12) the bounds on ℓ and m' are the same as in eqns. (8) and (9).

3 Numerical study of expansion accuracy

3.1 Relative truncation error

In any numerical implementation, the summation over n in expansion (2) is truncated at level N , yielding an approximation $K_N(\mathbf{r})$ of kernel $K(\mathbf{r})$:

$$K_N(\mathbf{r}) = \frac{ik}{4\pi} \sum_{n=0}^N \sum_{m=-n}^n (2n+1) (-1)^m I_n^{-m}(k, \mathbf{r}_y) O_n^m(k, \mathbf{r}_x) \quad (13)$$

The accuracy of (13) has been analysed e.g. by Song, Lu and Chew (1997) for the specific case of real wavenumbers ($\alpha = 1, \beta = 0$), $r_x \gg r_y$ and $\hat{\mathbf{r}}_x \cdot \hat{\mathbf{r}}_y = 1$. Empirical formulas for the choice of N have been proposed in order to guarantee a chosen level of accuracy on the evaluation of $K(\mathbf{r})$. For instance, it is found that

$$N = \vartheta r_y + M \log(\pi + \vartheta r_y) \quad (14)$$

should guarantee a relative error $E = |K - K_N|/|K|$ of 10^{-3} with $M = 3$, and $E = 10^{-6}$ with $M = 5$. Numerical evaluation of the truncation error E , displayed in Fig. 1 as isovalues of $\log(E)$ in a $(\vartheta r_y, N)$ -plane, leads to essentially the same conclusions as (14). On the basis of such results it is generally concluded and accepted that expansion (13) is not suited for efficient numerical implementations in the presence of moderate to high frequencies, for which a plane-wave expansion of $K(\mathbf{r})$ in diagonal form is usually preferred (see e.g. Darve, 2000a,b for Maxwell equations and Chaillat, Bonnet and Semblat, 2008 for elastodynamics).

In the case of complex wavenumbers of interest herein, the situation somewhat improves, as the truncation level N needed to reach a given kernel accuracy E is seen, on comparing Figs. 2 to 6, to decrease with increasing β . However, Figs. 2–6 also show that, for given $\beta > 0$, N still should be adjusted as a function of ϑd .

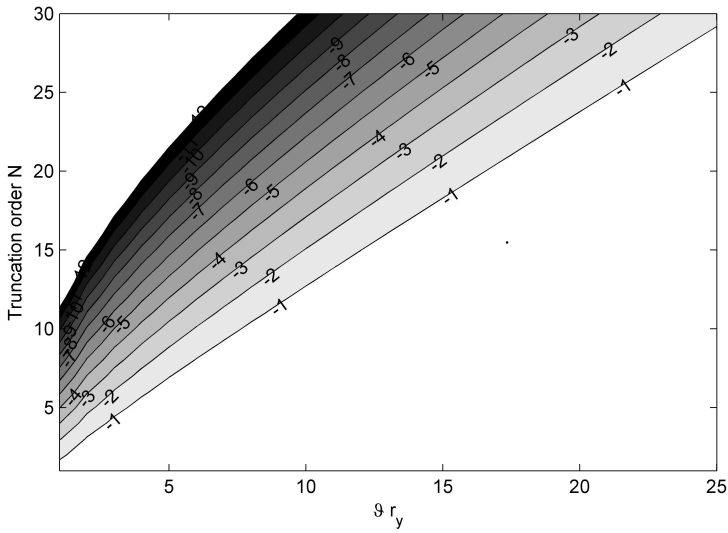


Figure 1: Isovalues of $\log(E)$, case $|\alpha| = 1, \beta = 0$ (purely-oscillatory kernel)

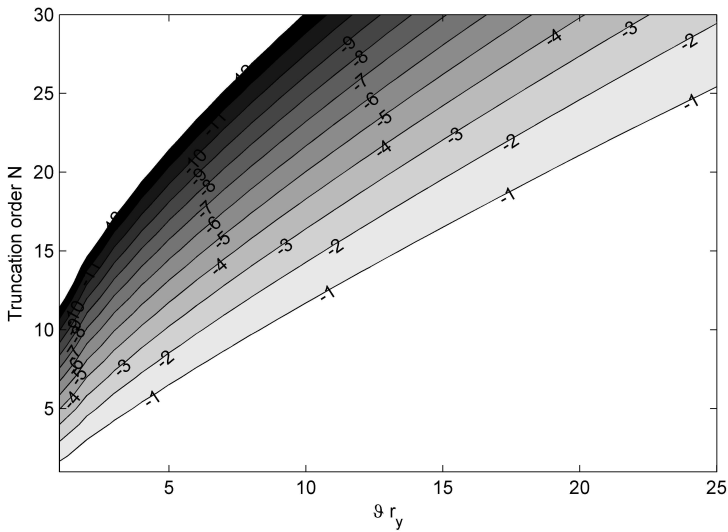


Figure 2: Isovalues of $\log(E)$, case $|\alpha| = 1, \beta = 0.1$

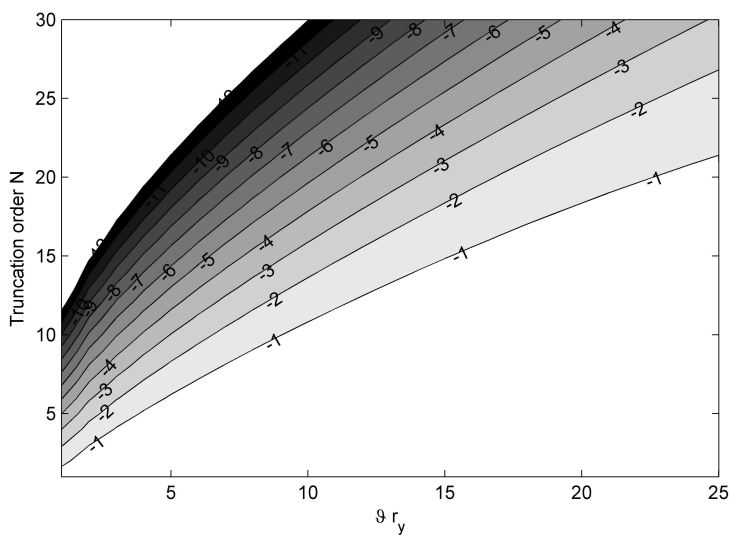


Figure 3: Isovalues of $\log(E)$, case $|\alpha| = 1, \beta = 0.2$

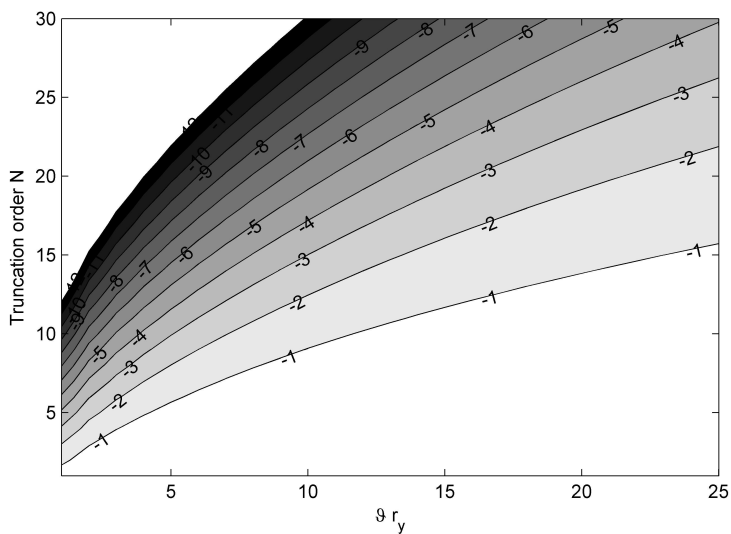


Figure 4: Isovalues of $\log(E)$, case $|\alpha| = 1, \beta = 0.5$

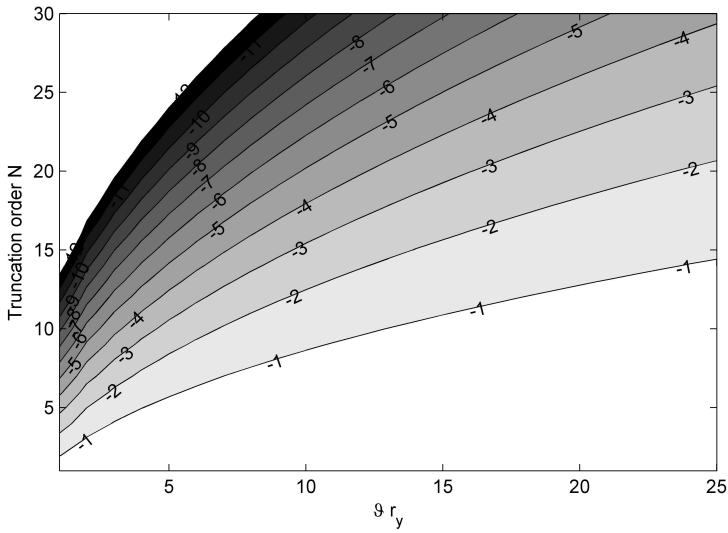


Figure 5: Isovalues of $\log(E)$, case $|\alpha| = 1, \beta = 1$

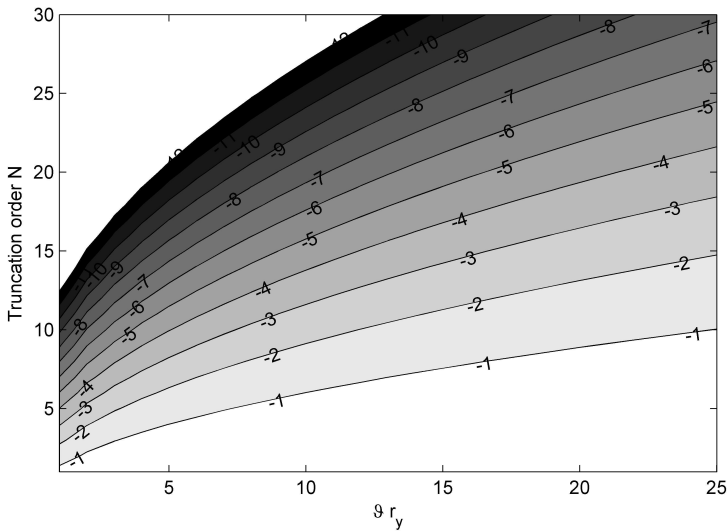


Figure 6: Isovalues of $\log(E)$, case $|\alpha| = 0, \beta = 1$ (purely-decaying kernel).

3.2 Weighted relative truncation error

The foregoing analysis, however, does not take into account that $K(\mathbf{r})$ decays exponentially with $\|\mathbf{r}\|$ if $\beta > 0$. For this reason, the relative accuracy E achieved on $K(\mathbf{r})$ may not be the most useful indicator, as it does not take into account the absolute relevance of the contribution of field points far from the collocation in the presence of dissipative terms. For this reason, an alternative line of reasoning is now proposed. Since for large values of $\beta \vartheta r$ the decaying term dominates in (1), it is natural to investigate the relative kernel error in a way that takes into account the absolute contribution of the kernel to the overall evaluation of integral operators. This suggests to consider the pointwise weighted error

$$E_M = E \exp^{-\beta \vartheta 2d} \tag{15}$$

instead of the standard relative error E . The chosen value $2d$ of the characteristic length in (15) is motivated by the observation, commonly made about FMM implementations, that the most severe errors in the application of (13) occur when the collocation point lies in a cell \mathcal{C}_x and the integration element lies in a cell \mathcal{C}_y of the interaction list of \mathcal{C}_x closest to \mathcal{C}_x (as in Fig. 7). Accordingly, this worst-case cell and source/collocation point configuration (Fig. 7) is now considered. Placing the expansion origin \mathbf{O} at the origin of Cartesian coordinates, let $\mathbf{x} = (-3d, 0, 0)$ and $\mathbf{y} = (-d, 0, 0)$, where $2d$ denotes the length of a cell side.

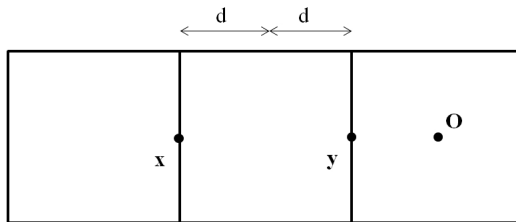


Figure 7: Choice of pole, source point, integration point

In what follows, the truncated series (1) is computed for different values of parameters d and N , and the weighted error E_M is numerically evaluated. Several specific values of α and β , chosen so as to be representative of the main physical models employing kernel $K(\mathbf{r})$ are considered. Ranges for (d, N) are adjusted so as to expose the interesting features of $E_M(d, N)$ for each choice of α, β . Results are collected in Figs. 8–13.

As can be appreciated from Figs. 12–13, for $|\alpha| \leq \beta$ the largest weighted error occurs at $\vartheta d = 0$ and, for instance, $N = 12$ guarantees $\log(E_M) \leq -6$ while $N = 8$ is

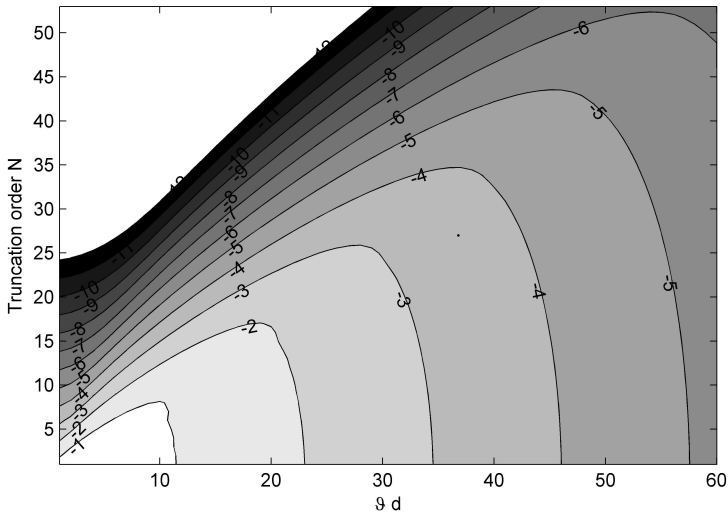


Figure 8: Isovalues of $\log(E_M)$ for $|\alpha| = 1, \beta = 0.1$.

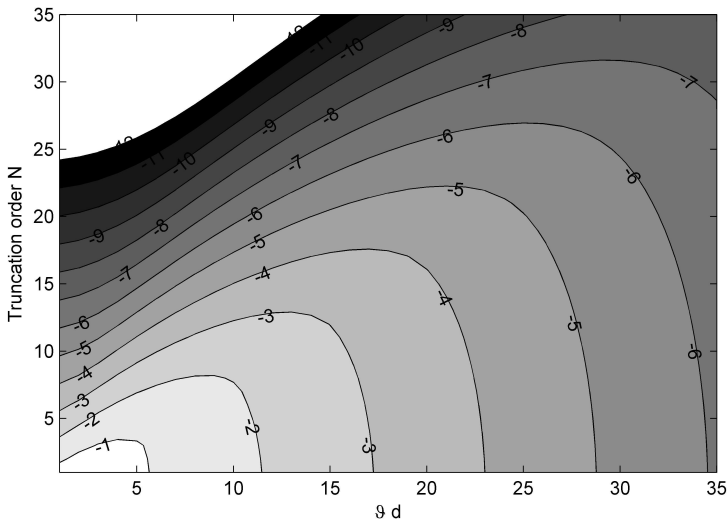


Figure 9: Isovalues of $\log(E_M)$ for $|\alpha| = 1, \beta = 0.2$.

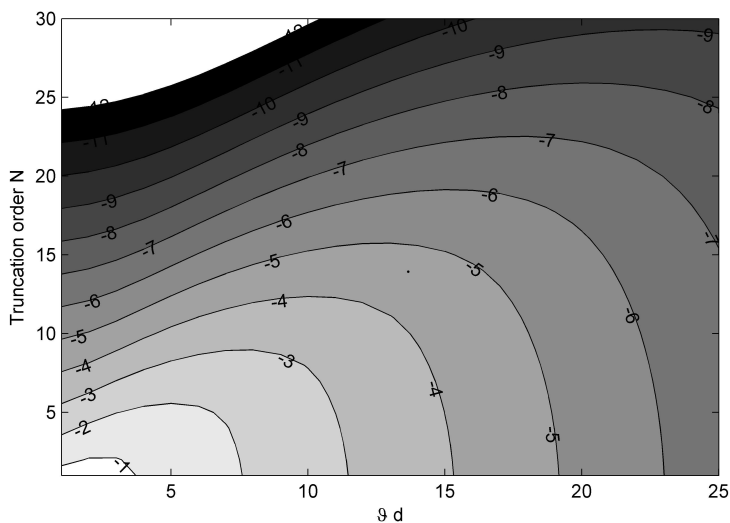


Figure 10: Isovalues of $\log(E_M)$ for $|\alpha| = 1, \beta = 0.3$.

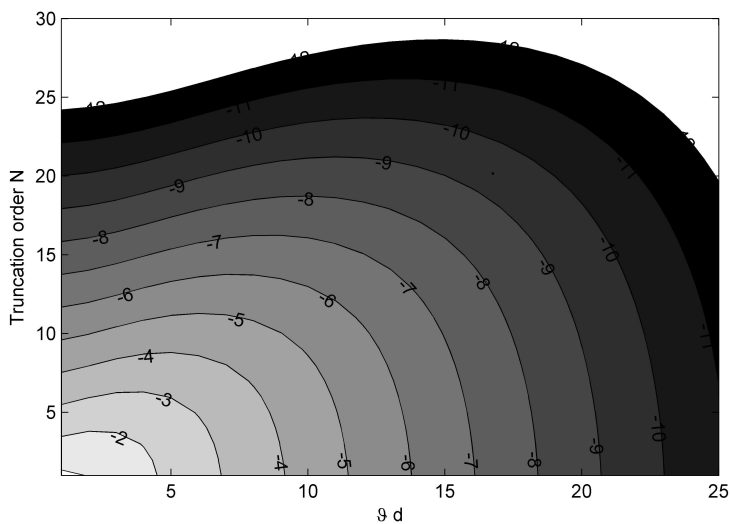


Figure 11: Isovalues of $\log(E_M)$ for $|\alpha| = 1, \beta = 0.5$.

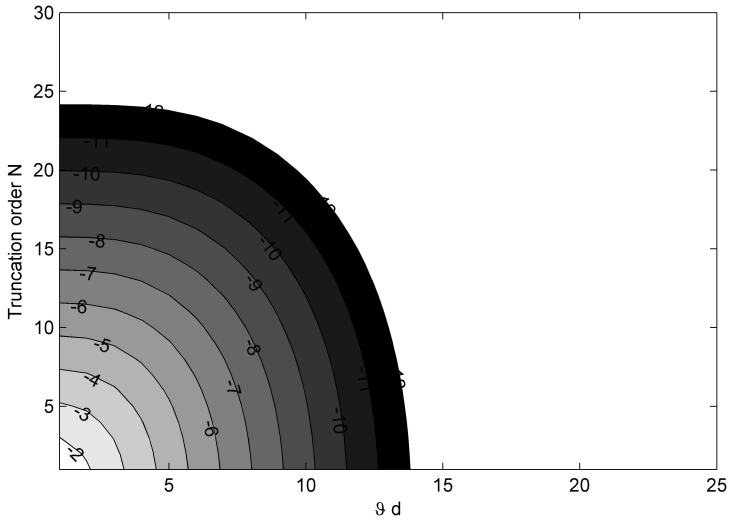


Figure 12: Isovalues of $\log(E_M)$ for $|\alpha| = 1, \beta = 1$.

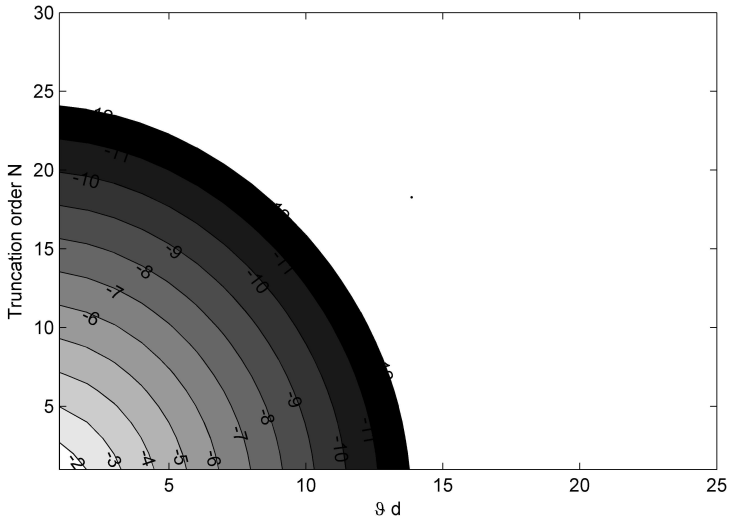


Figure 13: Isovalues of $\log(E_M)$ for $\alpha = 0, \beta = 1$.

sufficient for ensuring $\log(E_M) \leq -4$. For $\beta < 1$ (Figs. 8–11), one can still identify the truncation order N such that E_M is controlled and less than a prescribed amount, independently of ϑd , but this threshold now depends on β . Based on the results plotted in Figs. 8–12, a law of the form $N = c_1 + c_2\beta^{c_3}$ is sought, with its coefficients c_i identified by means of standard optimization routines. It is for instance found using this procedure that $\log(E_M) = -6$, $\log(E_M) = -4$ and $\log(E_M) = -3$ can be achieved using N_6 , N_4 and N_3 terms, respectively, with:

$$N_6 = 10.1 + 1.68\beta^{-1.4} \quad (16a)$$

$$N_4 = 6.7 + 1.15\beta^{-1.4} \quad (16b)$$

$$N_3 = 5.28 + 0.65\beta^{-1.5} \quad (16c)$$

The above empirical formulas are valid for $0.1 \leq \beta \leq 1$. One sees that for small values of β , high truncation orders are required to ensure a reasonable value of E_M . For instance, in the case $\alpha = 1, \beta = 0.1$, which might be of interest in viscoelasticity, ensuring $E_M \leq 10^{-3}$ requires $N = 26$. In contrast, for the case $\alpha = -1, \beta = 1$, typical of oscillatory Stokes flow and eddy currents, $N = 12$ achieves $E_M \leq 10^{-6}$. Similar conclusions are reached for the purely decaying case $\alpha = 0, \beta = 1$.

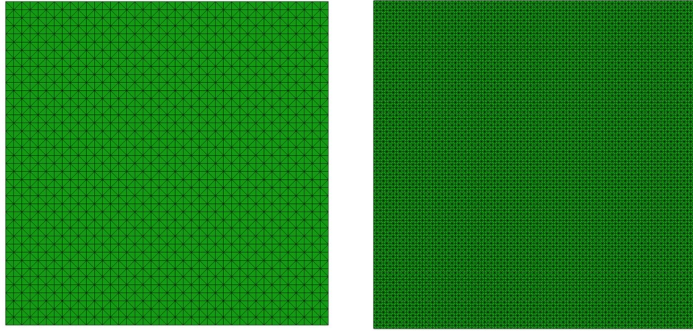
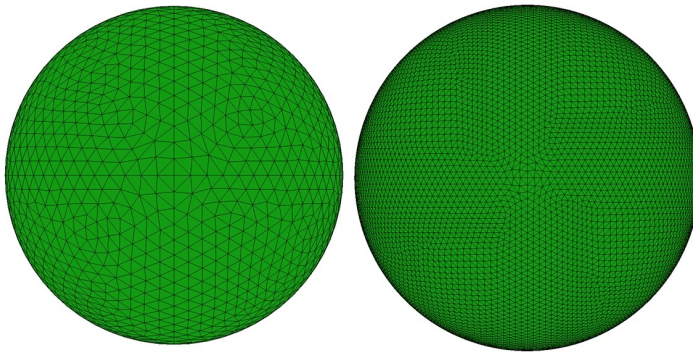
4 Full scale tests

In this section, we investigate whether the analysis carried out in Sec. 3.2 on the pointwise weighted error E_M allows to obtain practical guidelines for the choice of the truncation order N in general analyses. To this aim, full-scale tests are performed on a square plate of side $L = 10$ and a spherical surface of radius $R = 10$ both discretized employing 3-noded triangular plane boundary elements. For a selected collocation point (located at the square centre for the plate) the following integral, corresponding to a single-layer potential with constant density, is evaluated over the surface \mathcal{S} of the plate or sphere:

$$I = \int_{\mathcal{S}} e^{-\beta\vartheta r} \frac{e^{i\alpha\vartheta r}}{4\pi r} dS \quad (17)$$

The square plate is discretized with a fine mesh P_1 of 20000 elements and a coarse mesh P_2 of 3200 elements. The typical element size (defined as the square root of element area) is 0.07 for mesh P_1 and 0.177 for mesh P_2 . Similarly, the sphere is discretized with a fine mesh S_1 of 18668 elements (with typical element size 0.26) and a coarse mesh S_2 of 3076 elements (with typical element size 0.5).

For each test case, integral (17) is evaluated using two methods, namely (a) a standard BEM approach whereby all element integrals are computed directly, and (b) the standard FMM based on truncated expansion (1), as described in Greengard

Figure 14: Square plate: meshes P_1 and P_2 Figure 15: Sphere: meshes S_1 and S_2

and Rokhlin (1987, 1997). In both methods, the direct singular or nearly-singular integrals are evaluated by means of a classical semi-analytical procedure in which the “static” kernel $K^0(\mathbf{r})$ (i.e. the limit for $\vartheta \rightarrow 0$ of $K(\mathbf{r})$) is subtracted from $K(\mathbf{r})$ and then added back. The difference $K(\mathbf{r}) - K^0(\mathbf{r})$, being nonsingular for $\|\mathbf{r}\| = 0$, is integrated by means of a 7-point Gauss-Hammer numerical quadrature, while the singular static part $K^0(\mathbf{r})$ is integrated analytically as described in Milroy, Hinduja and Davey (1997). For all the non-singular, well-separated integrations, the 7-point Gauss-Hammer numerical quadrature is applied directly to $K(\mathbf{r})$. In the octree generation procedure used for the FMM evaluations, the maximum number of elements in a leaf is set to 50 and an adaptive octree is produced. For the four meshes of interest herein the number of levels in the octree structure, the minimum half-width d_{\min} and maximum half-width d_{\max} of cells contributing to the FMM are collected in Table 1.

The relative difference E_F between the standard and FMM evaluations of I is computed and plotted in Figs. 16–21 for the four meshes of interest and several choices

Mesh	levels	d_{\min}	d_{\max}
P_1	6	$5/(2^5) = 0.156$	$5/(2^2) = 1.25$
P_2	4	$5/(2^3) = 0.625$	$5/(2^2) = 1.25$
S_1	5	$10/(2^4) = 0.625$	$10/(2^2) = 2.5$
S_2	4	$10/(2^3) = 1.25$	$10/(2^2) = 2.5$

Table 1: Octree properties of the different surface meshes analysed

of β . It is of interest to determine whether the point-wise weighted error E_M introduced in Sec. 3.1 can be used to estimate *a priori* the actual relative error E_F caused by the FMM procedure relative to the direct computation of integrals (17). To this end, the maximum point-wise weighted error E_M induced by using a given truncation level N in (13) can be extrapolated from Figs. 8–13, by simple inspection, taking into account that the values of ϑd occurring during the FMM procedure are bounded according to $\vartheta d_{\min} \leq \vartheta d \leq \vartheta d_{\max}$, and compared to E_F .

Let us focus, e.g., on Fig. 19, which plots E_F for mesh P_2 , $N = 10$ as a function of ϑ for different combinations of α and β . For $\vartheta \rightarrow 0$ all the curves converge, which is expected since all the kernels tend to the common static limit. The situation is however different for increasing values of ϑ . For given mesh, ϑ , α and β , the segment $\{\vartheta d_{\min} \leq \vartheta d \leq \vartheta d_{\max}, N = 10\}$ can be drawn in the relevant plot of $E_M(\vartheta d, N)$ (Figs. 8-13). It can be reasonably argued that an upper bound for E_F could be estimated by picking the largest E_M along that segment.

For instance, consider the case $\alpha = 1, \beta = 1$ which corresponds to e.g. oscillatory Stokes flows or eddy currents. The weighted point-wise error E_M for this case is plotted in Fig. 12 and a maximum value of $\log(E_M) \approx -3.5, -5.3, -7.1$ is predicted for $N = 6, 10, 14$, respectively. Moreover the maximum value of $\log(E_M)$ for given N occurs for $\vartheta = 0$. This, according to the criterion introduced above, explains the behaviour of E_F in Fig. 19 for $\alpha = 1, \beta = 1$: the maximum of $E_F(\vartheta; N = 10)$ occurs for a small ϑ and is slightly overestimated by $\max_{\vartheta} E_M(\vartheta d, N = 10)$, and $E_F(\vartheta; N = 10)$ decreases as ϑ increases beyond the maximum point. Similar observations are made for the non-oscillatory exponential kernel ($\alpha = 0, \beta = 1$). The most important practical conclusion for the two cases $\alpha = 0$ or $1, \beta = 1$ is that the classical FMM based on expansion (1) with a fixed truncation order N , say $N = 10$, is expected to work satisfactorily and accuracy improves for large values of ϑ .

The situation is found to be different, as expected, for smaller values of β , but can still be predicted with the help of E_M . The relative error $E_F(\vartheta; N)$ initially increases with ϑ until a plateau is reached, a behavior qualitatively similar to that observed in the $\log(E_M)(\vartheta, N)$ plots of Figs. 8–11. Once again, E_M is found in

all cases considered here to conservatively estimate the maximum error E_F with respect to ϑ for given N . For instance, let us consider the case $\alpha = 1, \beta = .5$, again for the test case of Fig. 19 for which $N = 10$, with the corresponding plot of E_M in Fig. 11. Starting from $\vartheta = 0$, the function $E_M(\vartheta, N = 10)$ increases, reaches a maximum of $\log(E_M) = -4.6$ and then decreases. This compares very well with the situation depicted in Fig. 19, where the error $E_F(\vartheta; N = 10)$ increases, reaches a maximum of $\log(E_F) = -4.8$ and decreases. Very similar remarks could be presented for other combinations of parameters. It is however worth stressing that unless very small frequencies (or characteristic lengths) are of interest, small values of the dissipation coefficient β require high truncation orders N to keep E_F within acceptable limits, making the application of expansion (13) too expensive.

A very simple rule of thumb naturally stems from these remarks. Once α, β (i.e. the physical problem of interest) and the desired accuracy $E_F = \bar{E}$ are selected, the truncation order can be estimated in a conservative way from the relevant contour plot of $E_M(\vartheta, N)$ as the smallest truncation order N_{EF} such that the entire level curve $E_M = \bar{E}$ lies below the line $N = N_{EF}$.

Finally, a slightly modified test is performed by replacing the constant density by the oscillatory density $\cos(5x_1)\cos(5x_2)$ in the test surface integral I of Eq. (17), $x_1 = x_2 = 0$ being the center of the plate:

$$I = \int_{\mathcal{S}} e^{-\beta\vartheta r} \frac{e^{i\alpha\vartheta r}}{4\pi r} \cos(5x_1)\cos(5x_2) dx_1 dx_2 \quad (r^2 = x_1^2 + x_2^2) \quad (18)$$

The results for mesh P_1 , collected in Fig. 22, do not reveal major differences with respect to the uniform density case (Fig. 17).

5 Conclusions

The numerical parametric studies reported in this article yield useful guidelines for implementing and running FMM analyses based on the multipole expansion of the Helmholtz kernel with complex wavenumber. The most important conclusions drawn on that basis are:

1. When the dissipation parameter takes significant values (roughly $\beta \geq 0.5$), a range that covers the frequency-domain versions of parabolic equations governing e.g. Stokes flows, heat diffusion and eddy currents, a fixed truncation level $N \sim 10$ ensures both acceptable accuracy in the evaluation of single-layer potentials based on the Helmholtz kernel and acceptable computational costs. Conversely, N increases as β decreases, making this version of the FMM potentially too-expensive for low dissipation levels.

2. The weighted error E_M is found to provide a conservative estimate of the actual truncation error E_F occurring in the evaluation of a single-layer potential. This is useful e.g. for preliminary studies aiming at formulating selection rules for computational parameters such as N , as E_M is defined in terms of the kernel at isolated points and is therefore easier to implement and cheaper to evaluate than E_F .

It is however suggested that one use these guidelines as a basis for ad-hoc refinement according to the specific situation to be analysed, which may involve the Helmholtz kernel in a complex way (through its derivatives, or a tensorial construct) and integral operators more complex than single-layer potentials. The weighted error E_M applied to more complex dissipative kernels of Helmholtz-type is expected to prove a valuable tool for this purpose. Finally, it is hoped that future mathematical studies will address the formal truncation error analysis in the complex-wavenumber case.

Acknowledgement: Support from MIUR - PRIN07, grant 2007YZ3B24, is kindly acknowledged

References

- Abramowitz M.; Stegun I.** (1964): *Handbook of Mathematical Functions with Formulas, Graphs, and Mathematical Tables*. Dover.
- Bapat, M. S. and Shen, L. and Liu, Y. J.** (2009): Adaptive fast multipole boundary element method for three-dimensional half-space acoustic wave problems. *Eng. Anal. Boundary Elem.*, vol.33, 1113–1123..
- Casimir H.B.G.** (1948): On the attraction between two perfectly conducting plates. *Proc. K. Ned. Akad. Wet.*, vol.60, 793–795..
- Chaillat S.; Bonnet M.; Semblat J.F.** (2008): A multi-level fast multipole BEM for 3-D elastodynamics in the frequency domain. *Comp. Meth. Appl. Mech. Eng.*, vol.197, 4233–4249.
- Darve E.** (2000): The Fast Multipole Method : Numerical Implementation. *J. Comput. Phys.*, vol.160, 195–240.
- Darve E.** (2000): The fast multipole method: I. Error analysis and asymptotic complexity. *SIAM J. Numer. Anal.*, vol.38, 98–128.
- Dominguez J.** (1993): *Boundary Elements in Dynamics*. Computational Mechanics Publications and Elsevier Science.
- Epton M.A.; Dembart B.** (1995): Multipole translation theory for three-dimensional Laplace and Helmholtz equations. *SIAM J. Sci. Comput.*, vol.16, 865–897.

- Frangi A.** (2005): A fast multipole implementation of the qualocation mixed-velocity-traction approach for exterior Stokes flows. *Eng. Anal. Boundary Elem.*, vol.29, 1039–1046.
- Frangi A.; Ghezzi L.; Faure-Ragani P.** (2006): Accurate Force Evaluation for Industrial Magnetostatics Applications with Fast BEM-FEM Approaches. *Comput. Model. Eng. Sci.*, vol.15, 41–48.
- Frangi A; Spinola G.; Vigna B.** (2006): On the evaluation of damping in MEMS in the slip-flow regime. *Int. J. Num. Meth. Eng.*, vol.68, 1031–1051.
- Fu Y.; Rodin G.J.** (2000): Fast solution method for three-dimensional Stokesian many-particle problems.. *Comm. Num. Meth. Eng.*, vol.16, 145–149.
- Geng N., Sullivan A. and Carin, L.** (2001): Fast multipole method for scattering from an arbitrary PEC target above or buried in a lossy half space.. *IEEE Trans. Antennas Propag.*, vol.49, 740–748.
- Greengard L.; Rokhlin V.** (1987): A fast algorithm for particle simulations. *J. Comput. Phys.*, vol.73, 325–348.
- Greengard L.; Rokhlin V.** (1997): A new version of the fast multipole algorithm for the Laplace equation in three dimensions. *Acta Numerica*, vol.6, 229–269.
- Gumerov, N. A., Duraiswami, R.** (2005): *Fast multipole methods for the Helmholtz equation in three dimensions*. Elsevier.
- Messiah, A.** (1968): *Quantum mechanics*. Wiley.
- Milroy J.S.; Hinduja S.; Davey K.** (1997): The elastostatic three dimensional boundary element method: analytical integration for linear isoparametric triangular elements. *Appl. Math. Modelling*, vol.21, 763–782.
- Nishimura N.; Yoshida K.; Kobayashi S.** (2001): Application of fast multipole Galerkin boundary integral equation method to elastostatic crack problems in 3D. *Int. J. Num. Meth. Eng.*, vol.50, 525–547.
- Nishimura N.** (2002): Fast multipole accelerated boundary integral equation methods. *Appl. Mech. Rev.*, vol.55, 299–324.
- Reid H.; Rodriguez A.W.; White J.; Johnson S.G.** (2009): Efficient computation of Casimir interactions between arbitrary 3D objects. *Phys. Rev. Lett.*, vol.103, 040401—.
- Rokhlin V.** (1985): Rapid solution of integral equations of classical potential theory. *J. Comput. Phys.*, vol.60, 187–207.
- Schmidlin G.; Fischer U.; Andjelic Z. and Schwab C.** (2001): Preconditioning of the second-kind boundary integral equations for 3D eddy current problems. *Int. J. Num. Meth. Eng.*, vol.51, 1009–1031.

Song J.; Lu C-C.; Chew W.C. (1997): Multilevel Fast Multipole Algorithm for Electromagnetic Scattering by Large Complex Objects. *IEEE Trans. Antennas Propag.*, vol.45, 1488–1493.

Yasuda Y. and Sakuma T. (2008): Analysis of sound Fields in Porous Materials Using the Fast Multipole BEM, *37th International Congress and Exposition on Noise Control (Inter-noise 2008)*, Shanghai, China.

Ye W.; Wang X.; Hemmert W.; Freeman D.; White J. (2003): Air damping in lateral oscillating micro-resonators: a numerical and experimental study. *Journal of Microelectromechanical Systems*, vol.12, 557–566.

Yoshida K. (2001): Applications of Fast Multipole Method to Boundary Integral Equation Method, *Ph.D. Thesis*, Kyoto University.

Zacharopoulos, A.D., Arridge S.R., Dorn O., Kolehmainen V. and Sikora J. (2006): Three dimensional reconstruction of shape and piecewise constant region values for Optical Tomography using spherical harmonic parameterisation and a Boundary Element Method. *Inverse Problems*, vol.22, 1509–1532.

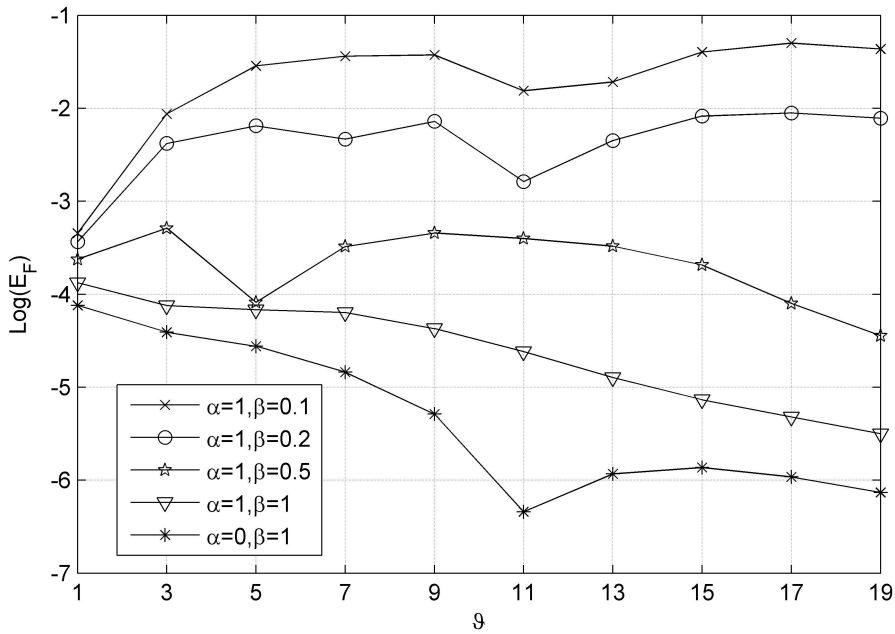


Figure 16: Plate, mesh P_1 , truncation order $N = 6$

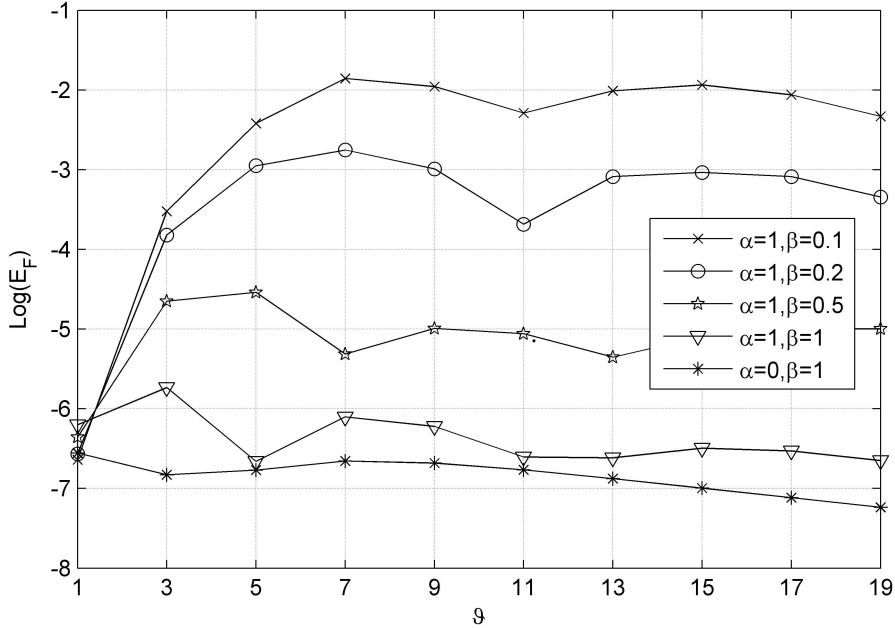


Figure 17: Plate, mesh P_1 , truncation order $N = 10$

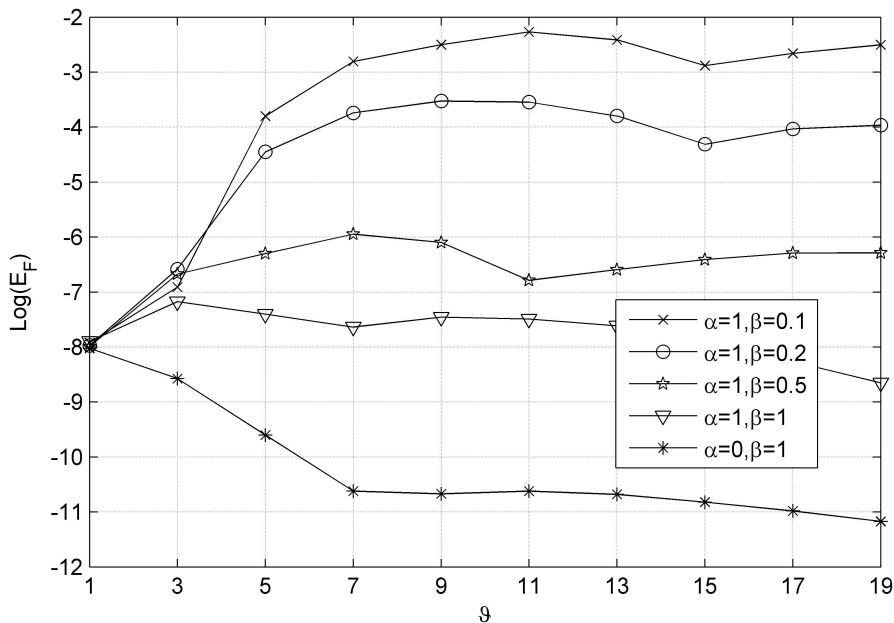


Figure 18: Plate, mesh P_1 , truncation order $N = 14$

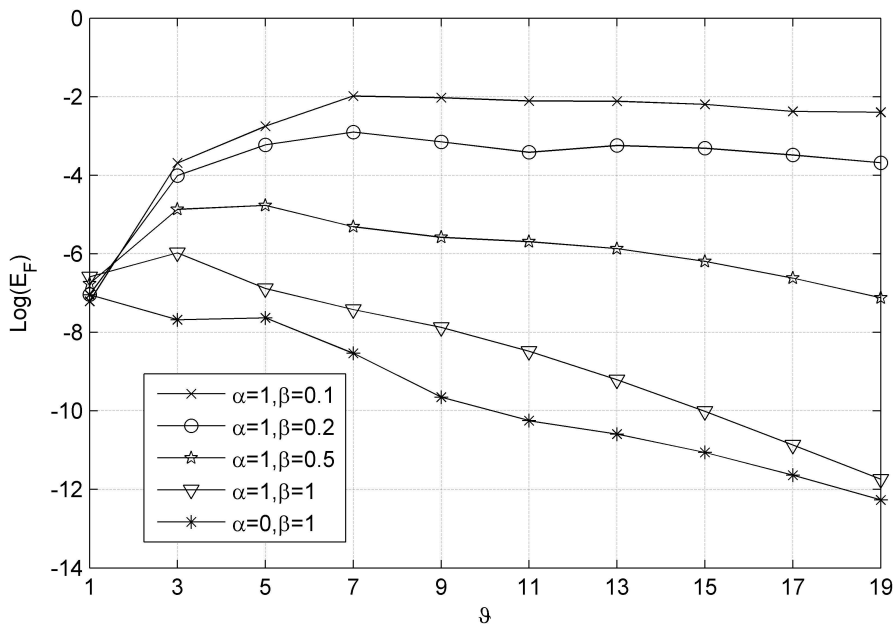


Figure 19: Plate, mesh P_2 , truncation order $N = 10$

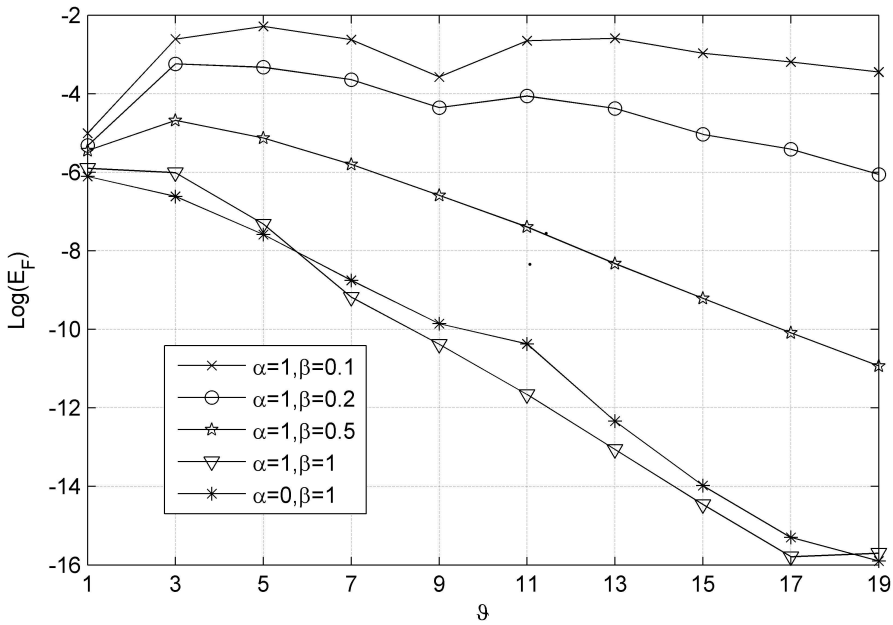


Figure 20: Sphere, mesh S_1 , truncation order $N = 10$

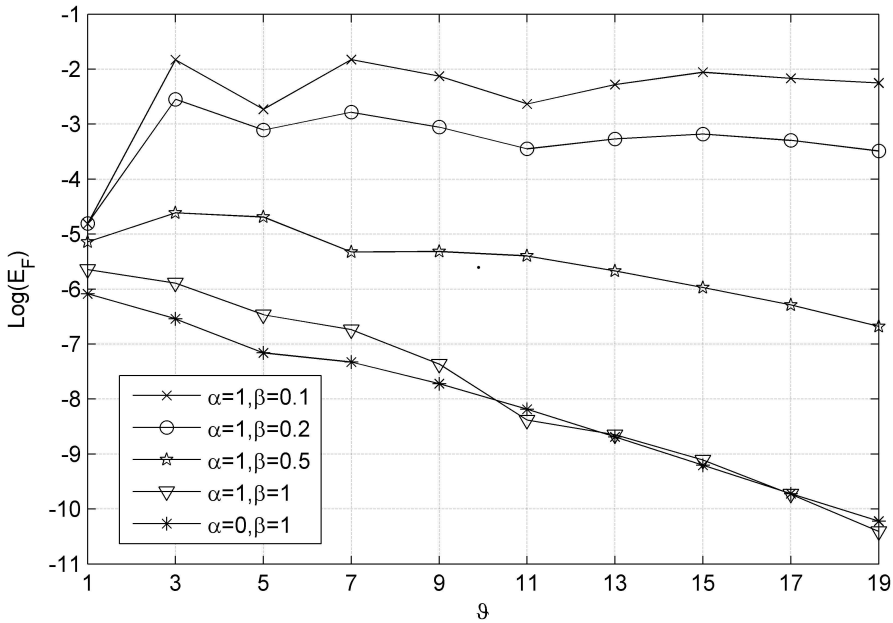
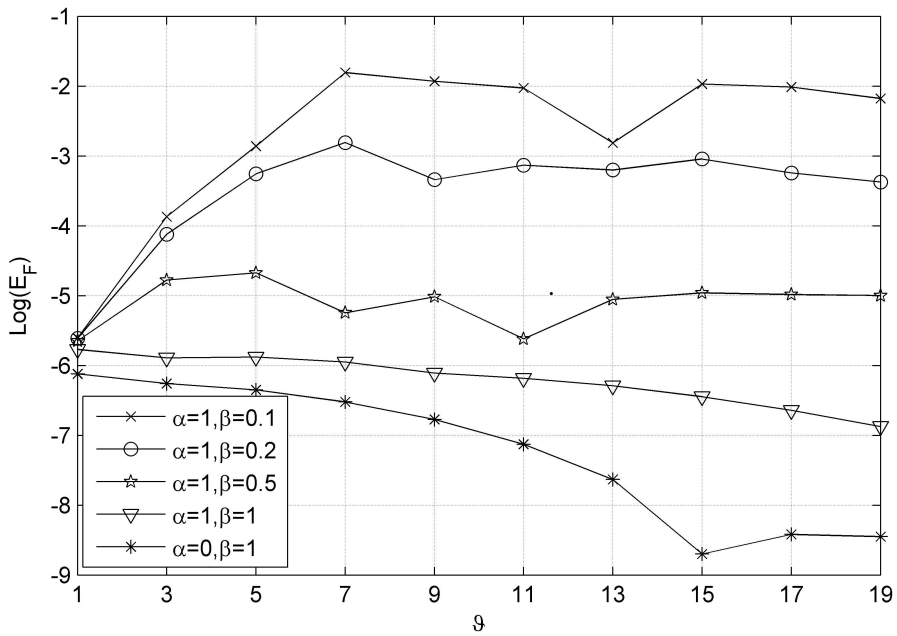


Figure 21: Sphere, mesh S_2 , truncation order $N = 10$

Figure 22: Plate, mesh P_1 , truncation order $N = 10$, non-uniform density

